Revista Internacional de Investigación e Innovación Tecnológica

Página principal: www.riiit.com.mx

Microstructural effects of preconditioning materials on gray iron and their impact on corrosion resistance

Efecto microestructural de materiales preacondicionadores en hierro gris y su impacto en la resistencia a la corrosión

Villarreal-Fuentes, B.O.[a], Rodríguez-Reyes, M.[a]*, Vázquez-Obregón, D.[b], Sánchez-Arroyo, A.[a], Olvera-Romero, G.D.[c], Veloza-Matamoros, Z.[a], Zamora-García, J.J.[b], Acevedo-Dávila, J.L.[b]

[a] División de Estudios de Posgrado e Investigación; Tecnológico Nacional de México / Instituto Tecnológico de Saltillo; C.P. 25280, Saltillo, Coahuila, México. ORCID: https://orcid.org/0009-0003-8933-5105, https://orcid.org/0009-0009-5977-3116*, https://orcid.org/0009-0005-7095-2677, https://orcid.org/0000-0002-3958-3157.

[b] Departamento de Metal-Mecánica; Tecnológico Nacional de México / Instituto Tecnológico de Saltillo; C.P. 25280, Saltillo, Coahuila, México. ORCID: https://orcid.org/0009-0007-4830-3763, https://orcid.org/0009-0003-4740-3202, https://orcid.org/0000-0002-2439-2649.

[c] Facultad de Ingeniería; Universidad Autónoma de Coahuila; C.P. 25350, Arteaga, Coahuila, México. ORCID: https://orcid.org/0000-0002-0885-1761.

d22050001@saltillo.tecnm.mx; mario.rr@saltillo.tecnm.mx*; dagoberto.vo@saltillo.tecnm.mx; m20051903@saltillo.tecnm.mx; golvera@uadec.edu.mx; zully.mv2@saltillo.tecnm.mx; jose.zg@saltillo.tecnm.mx; jorge.ad@saltillo.tecnm.mx

Technological innovation: Improved microstructural effects and reduced gray iron corrosion.

Industrial application area: Metallurgical and automotive industries.

Received: November 21, 2025
Accepted: July 21, 2026

Resumen

La corrosión de los discos de freno de hierro gris en ambientes agresivos representa un desafío creciente para la industria automotriz, particularmente en los vehículos híbridos y eléctricos, donde la menor frecuencia de frenado favorece los procesos de degradación por corrosión. Este fenómeno no solo afecta el desempeño y la vida útil de los componentes, sino que también contribuye a la emisión de material particulado con potencial impacto sobre la salud humana y el medio ambiente. El presente estudio evaluó la influencia de tres materiales preacondicionadores (grafito metalúrgico, grafito de electrodo y coque metalúrgico) sobre la microestructura y la resistencia a la corrosión del hierro gris. Se realizaron tres coladas independientes bajo condiciones idénticas

de fusión a 1450 °C, empleando cada material preacondicionador por separado. De cada colada se obtuvieron tres probetas para la caracterización microestructural y electroquímica. La cuantificación microestructural se realizó mediante análisis de imágenes utilizando diez mediciones por condición experimental para determinar la fracción de perlita fina, la densidad de inclusiones de MnS y el espaciamiento interlaminar de la perlita. La resistencia a la corrosión se evaluó mediante ensayos de polarización potenciodinámica en una solución de NaCl al 3.5% en peso, utilizando una velocidad de barrido de 0.1667 mV/s y un intervalo de potencial de ±0.5 V respecto al potencial de corrosión. Se realizaron cinco mediciones por probeta y los resultados reportados corresponden al valor promedio. Las diferencias entre las condiciones experimentales se evaluaron mediante un análisis de varianza de una vía (ANOVA), encontrándose diferencias estadísticamente significativas ($p < 0.05$).

El hierro gris preacondicionado con coque metalúrgico presentó la mayor densidad de inclusiones de MnS (226 ± 5 MnS/mm²), la mayor fracción de perlita fina (55.35 ± 0.84%) y el menor espaciamiento interlaminar de la perlita (170 ± 3.50 nm). En correspondencia, esta aleación exhibió la menor densidad de corriente de corrosión y la menor velocidad de corrosión (0.016 ± 0.002 mm/año), lo que representa una reducción aproximada del 65% con respecto a la aleación preacondicionada con grafito de electrodo. Los resultados indican que la mejora en la resistencia a la corrosión está asociada con la influencia combinada del material preacondicionador seleccionado y de las condiciones metalúrgicas resultantes, incluidas las diferencias en el contenido de azufre, la relación Mn/S, el equivalente de carbono, la densidad de inclusiones de MnS y el refinamiento de la perlita. Estos hallazgos demuestran que una adecuada selección del material preacondicionador puede modificar el comportamiento de solidificación y la evolución microestructural del hierro gris, mejorando su desempeño frente a la corrosión en ambientes agresivos.

Palabras clave: Resistencia a la corrosión, Microestructura perlítica, Hierro gris, Materiales preacondicionadores.

Abstract

The corrosion of gray cast iron brake discs in aggressive environments is a growing concern for the automotive industry, particularly in hybrid and electric vehicles, where reduced brake usage promotes corrosion-related degradation. This phenomenon not only affects brake performance and service life but also contributes to particulate matter emissions with potential environmental and health impacts. The present study evaluated the influence of three preconditioning materials (metallurgical graphite, electrode graphite, and metallurgical coke) on the microstructure and corrosion resistance of gray cast iron. Three independent heats were produced under identical melting conditions at 1450 °C, using each preconditioning material separately. Three specimens were obtained from each heat for microstructural and electrochemical characterization. Quantitative image analysis was performed using ten measurements per experimental condition for the determination of the fine pearlite fraction, MnS inclusion density, and pearlite interlamellar spacing. Corrosion resistance was evaluated by potentiodynamic polarization in a 3.5 wt.% NaCl

solution using a scan rate of 0.1667 mV/s over a potential range of ±0.5 V with respect to the corrosion potential. Five measurements were performed for each specimen, and the reported values represent mean values. Statistical differences among the evaluated conditions were assessed by one-way ANOVA ($p < 0.05$).

The gray cast iron preconditioned with metallurgical coke exhibited the highest MnS inclusion density (226 ± 5 MnS/mm²), the largest fraction of fine pearlite (55.35 ± 0.84%), and the smallest pearlite interlamellar spacing (170 ± 3.50 nm). Correspondingly, this alloy exhibited the lowest corrosion current density and corrosion rate (0.016 ± 0.002 mm/year), representing an approximately 65% reduction compared with the alloy preconditioned using electrode graphite. The results indicate that the improved corrosion resistance is associated with the combined influence of the selected preconditioning material and the resulting metallurgical conditions, including differences in sulfur content, Mn/S ratio, carbon equivalent, MnS inclusion density, and pearlite refinement. These findings demonstrate that appropriate selection of the preconditioning material can modify the solidification behavior and microstructural evolution of gray cast iron, thereby improving its corrosion performance in aggressive environments.

Keywords: Corrosion resistance, Pearlitic microstructure, Gray iron, Preconditioning materials.

1. Introduction

Global vehicle sales were estimated at 77 to 89 million units in 2024 (1). This figure gives an indication of the scale of the design, manufacturing, and commercial activities associated with the automotive industry. The types of vehicles entering this market have also begun to change. Battery electric vehicles (BEVs), hybrid electric vehicles (HEVs), and plug-in hybrid electric vehicles (PHEVs) are becoming more common. Environmental concerns and the increasing cost of fossil fuels are among the factors behind this shift (2–5). In these vehicles, regenerative braking recovers some of the kinetic energy that would normally be lost during deceleration. This energy is converted into electricity and returned to the battery. Its recovery reduces energy losses and can increase the distance traveled between charges (6, 7).

Regeneration, however, does not eliminate the need for a friction brake. Both electric and conventional vehicles use friction braking systems, and a widely used arrangement pairs a gray cast iron disc with a composite pad. The pad may be manufactured from semimetallic or ceramic materials (8). Because this system directly affects braking performance, it must operate reliably under the various operating conditions encountered by vehicles. However, studies have shown that prolonged parking periods or exposure to aggressive environmental conditions can promote adhesion between the brake pad and disc surfaces, making brake release difficult and potentially reducing braking efficiency due to disc corrosion (8–10). Gray iron is the metal commonly used in brake discs, so it has been extensively studied to fulfill the purpose of braking, focusing on thermal and mechanical properties such as thermal conductivity, fatigue resistance and hardness (11–13). However, research into the corrosion resistance of this material has generated considerable interest among researchers in the metallurgical, environmental, and health sectors.

The corrosion of gray iron components not only leads to the deterioration of their mechanical and functional properties, potentially compromising braking performance, but also poses significant environmental and health concerns. During brake operation, corrosion products generated from iron-containing materials can be released into the environment, contributing to increased concentrations of airborne particulate matter (14, 15). Many of these particles have diameters below 100 nm. Their small size allows them to penetrate deep into the respiratory system and may facilitate their transport to other organs, including the brain. In addition to their size, their high bioreactivity represents a potential health concern because exposure to these particles has been associated with the development and progression of neurodegenerative conditions, including Parkinson's disease and Alzheimer's disease.

Several routes have been studied to reduce the corrosion of gray iron. These include the addition of alloying elements, the use of protective coatings, heat treatments that produce more stable microstructures, and the incorporation of reinforcing phases. Depending on the approach, corrosion resistance can be improved through changes in the surface condition or in the microstructure of the material. Bruna et al. (17) studied ferritic gray iron exposed to solutions representative of marine environments. Their results showed that additions of copper and nickel reduced the corrosion rate.

A. H. Seikh et al. (18) investigated copper additions to austempered gray iron. They identified ferrite, bainite, and austenite with a high carbon content in the resulting microstructure. Under the conditions examined, this material resisted corrosion better than conventional gray iron. A different method was reported in (19), where bone particles were added to gray iron as reinforcement. The authors related the improvement in corrosion resistance to the formation of a passive layer and to changes produced by microstructural refinement.

Lamellar graphite in gray iron is distributed through a matrix containing pearlite and ferrite. The relative amount of pearlite is particularly important because it contributes to the mechanical strength of the material. Pearlite formation is affected by the composition of the melt and by its cooling history. For this reason, both the metallic charge and the materials added during preconditioning, especially carburizers, can alter the final microstructure and properties of the casting (20, 21).

The present study compared different preconditioning materials and examined the changes associated with each one.

The study examined the changes in pearlite refinement, MnS formation, graphite nucleation, and corrosion behavior produced under each condition. A practical objective was to obtain the required properties during casting, without adding a later heat treatment. If this operation can be avoided, the production sequence becomes shorter and less costly. Better resistance to degradation may also reduce the release of fine particles while the material is in service. This possible environmental benefit was not measured directly in the present study.

2. Materials and equipment

Gray iron samples were produced using a medium-frequency induction furnace with a capacity of 5 kg. The chemical composition of the irons was determined by optical emission spectroscopy (OES) using a SPECTRO M11 spectrometer. Microstructural characterization was performed using a NIKON optical

microscope (OM) and a JEOL JSM-6610LV scanning electron microscope (SEM).

Metallurgical graphite (MG), electrode graphite (EG), and metallurgical coke (MC), all with particle sizes smaller than 800 μm, were used as preconditioning materials. The purity of these materials is presented in Table 1.

Table 1. Purity of preconditioning materials (wt%).

Pre-cond.	C	Humidity	Vol. Mat.	Ash	S
MG	98.50	0.22	1.32	1.32	0.02
EG	93.10	0.53	1.43	5.47	0.13
MC	83.51	0.57	2.65	13.84	0.50

The corrosion behavior of the different gray irons was evaluated by potentiodynamic polarization testing using an electrochemical cell equipped with a platinum mesh counter electrode and a saturated calomel electrode (SCE) as the reference electrode. Electrochemical measurements were performed using a Solartron SI 1287 Electrochemical Interface potentiostat/galvanostat system.

3. Experimental method

Three gray cast irons were produced using different preconditioning materials: metallurgical graphite, electrode graphite, and metallurgical coke. One independent heat was produced for each experimental condition under identical melting conditions using a 5 kg metallic charge. All melting operations were carried out at 1450 °C. After complete melting and homogenization, the liquid metal was poured into standard Shell sand thermal analysis cups to produce the test specimens, and three specimens were obtained from each heat for subsequent microstructural and electrochemical characterization.

The amount of preconditioning material added to each heat was adjusted according to the carbon balance required to obtain the target chemical composition. Specifically, additions of 0.81 wt.%, 0.86 wt.%, and 0.96 wt.% (relative to the 5 kg metallic charge) were employed for the melts preconditioned with metallurgical graphite, electrode graphite, and metallurgical coke, respectively. These additions were selected according to the carbon content and purity of each preconditioning material while maintaining identical melting parameters for all experimental conditions.

To promote gradual carbon dissolution and improve chemical homogenization, the total amount of preconditioning material was divided into three equal additions. Approximately one-third (33%) was introduced together with the initial metallic charge at the beginning of melting, the second third was added after approximately 50% of the metallic charge had melted, and the remaining third was incorporated once complete melting of the metallic charge had been achieved. Immediately after each addition, the molten bath was manually stirred to facilitate the incorporation and dissolution of the preconditioning material. This manual stirring was performed only at the time of each addition and was not maintained throughout the melting process. During the remainder of melting, bath homogenization was provided by the electromagnetic stirring naturally generated during induction melting. Following the final addition, the melt was maintained under homogenization conditions for 5–7 min before pouring.

The specimens were sectioned and metallographically prepared by progressive grinding using silicon carbide (SiC) abrasive papers with grit sizes from 120 to 1000, followed by polishing with a short-fiber cloth and 1 μm diamond paste. The polished surfaces were subsequently etched with a 2% Nital solution to reveal the microstructure.

Microstructural characterization was performed by optical microscopy (OM) according to ASTM A247 and the AFS 5-J classification for graphite morphology. Representative optical and scanning electron microscopy (SEM) images were acquired from randomly selected fields distributed throughout each specimen to minimize the influence of local microstructural heterogeneity. The pearlite interlamellar spacing was determined using the Underwood method (22), according to Equation (1):

$$S_t = \frac{\pi d_c}{4 n_c} \quad \textbf{(Eq. 1)}$$

where S_t is the pearlite interlamellar spacing, d_c is the diameter of the test circle superimposed on the pearlitic colony, and n_c is the number of ferrite/cementite lamellae intercepted by the diameter of the test circle.

Quantitative microstructural characterization was performed using ImageJ software. The fraction of fine pearlite was determined by area fraction analysis based on color thresholding of the etched optical micrographs, whereas the number density of MnS inclusions (inclusions MnS/mm²) was determined from SEM micrographs. For each experimental condition, ten measurements distributed among the three specimens were performed to determine the fine pearlite fraction, pearlite interlamellar spacing, and MnS inclusion density. The reported values correspond to the average of these measurements.

Corrosion resistance was evaluated by potentiodynamic polarization tests in accordance with ASTM G5 using a conventional three-electrode electrochemical cell containing a 3.5 wt.% NaCl solution at room temperature. Each electrochemical test used a platinum mesh as the counter electrode and a saturated calomel electrode (SCE) as the reference. Surface preparation consisted of grinding with 1000 grit SiC paper, followed by polishing and cleaning with distilled water and ethanol. The area exposed to the electrolyte was 1 cm². After immersion, the open circuit potential (OCP) was followed for 5 min before the polarization scan was started. Measurements were made from 0.5 V below Ecorr to 0.5 V above Ecorr using a scan rate of 0.1667 mV/s. Five curves were obtained under each experimental condition, and the reported electrochemical parameters are their average values. Tafel extrapolation was applied to the linear sections of the anodic and cathodic branches to determine the corrosion current density (Icorr) and corrosion potential (Ecorr). The slope for each branch was obtained from a separate linear fit of the corresponding section of the semilogarithmic curve.

The experimental procedure was designed as a comparative single-factor study, in which the type of preconditioning material was established as the primary processing variable, while all melting, specimen preparation, metallographic characterization, and electrochemical testing conditions were maintained constant. Although minor variations in the final chemical composition resulted from the intrinsic characteristics of each preconditioning material, the adopted experimental design enabled a systematic comparison of their influence on the microstructure and corrosion behavior of the gray cast irons.

4. Results and discussion

For clarity, the gray irons were identified according to the preconditioning material used. GI1 corresponds to metallurgical graphite, GI2 to electrode graphite, and GI3 to metallurgical coke. Their chemical compositions are listed in Table 2. Among the three alloys, GI1 had the highest carbon equivalent (C.E.), followed by GI2 and GI3. Gray iron castings intended for engineering applications commonly have carbon equivalent values between 3.0 and 4.5 wt.%. This range favors the mechanical and chemical characteristics expected from this type of cast iron (23). The calculated Mn/S ratios were 10 for GI1, 8 for GI2, and 5 for GI3. All three values are within the recommended interval of 5 to 15. Within this interval, conditions for MnS formation become more favorable as the ratio approaches the lower limit (24, 25).

GI3 had the lowest Mn/S ratio because metallurgical coke introduced more sulfur into the melt than metallurgical graphite or electrode graphite. Part of the sulfur contained in the coke was transferred to the molten metal during processing, resulting in a sulfur concentration of 0.08 wt.% in GI3 (20, 21). Sulfur is commonly classified as a residual element in cast iron. Its concentration, however, does not fully describe how it will affect the material because the amount of manganese available in the melt also has to be taken into account (26). GI3 had the highest sulfur content of the three alloys, but its Mn/S ratio did not fall outside the recommended interval for gray cast iron. The manganese present in this alloy was therefore sufficient for sulfur to combine preferentially as MnS, reducing the likelihood of forming harmful FeS phases (25).

Table 2. Chemical composition (wt%) of the different gray irons.

Gray Iron	C	Si	Mn	P	S	C.E	
GI1	3.19	1.96	0.38	0.03	0.04	3.90	10
GI2	2.86	1.90	0.40	0.05	0.05	3.50	8
GI3	2.75	1.85	0.37	0.03	0.08	3.40	5

4.1 Microstructure

4.1.1 Effect of preconditioners on microstructure

Figure 1 shows the microstructures of the GI1, GI2, and GI3 gray irons. All samples exhibited a predominantly pearlitic matrix containing Type E graphite. However, quantitative image analysis revealed differences in the fraction of fine pearlite among the evaluated systems.

A higher fraction of fine pearlite was observed in the GI3 system compared with GI1 and GI2. Quantitative phase analysis revealed fine pearlite fractions of 55.35 ± 0.84% for GI3, 51.00 ± 0.87% for GI1, and 49.18 ± 1.08% for GI2. Pearlite refinement has been widely associated with processing variables such as cooling rate and alloy chemistry. Lima et al. (27) reported that increasing the cooling rate promotes pearlite refinement, whereas additions of alloying elements such as Cu, Mo, and Cr further enhance this effect. Conversely, annealing treatments reduce the fraction of fine pearlite by promoting microstructural coarsening (28).

To better understand the formation of the pearlitic matrix and graphite structure, the nucleation mechanisms of both phases were analyzed. It is well established that during the solidification of gray iron, once the temperature falls below the eutectic

temperature, the microstructure consists of austenite (γ-iron with dissolved carbon) and graphite (29). As cooling progresses, the carbon dissolved in the austenitic matrix diffuses toward regions with higher carbon affinity and enhanced atomic mobility, such as graphite flakes and grain boundaries (30, 31). Under slow to moderate cooling conditions, when the eutectoid temperature is reached, the carbon remaining in solid solution within the matrix and not incorporated into the graphite flakes precipitates as cementite (Fe_3C). This process leads to the formation of pearlite, a lamellar microconstituent composed of alternating ferrite (α-iron) and cementite layers (32).

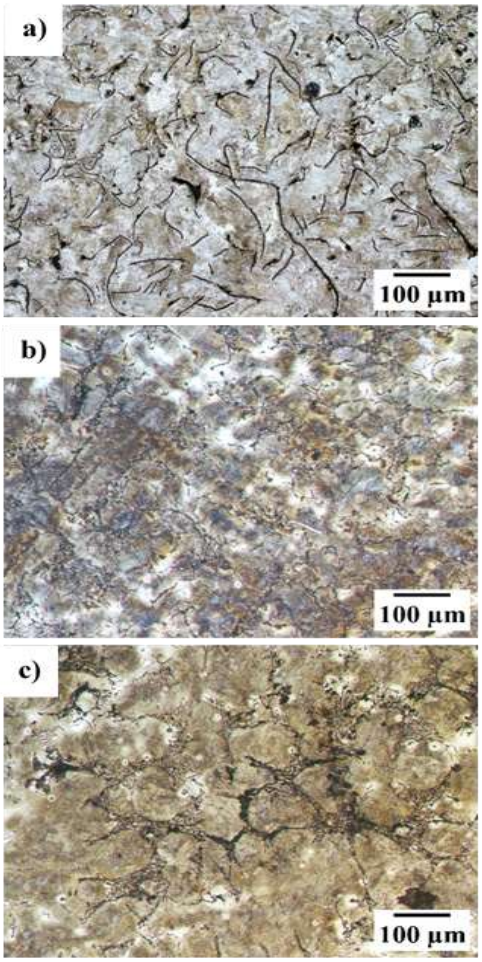

Figure 1. OM images of microstructures of gray irons a) GI1, b) GI2, and c) GI3.

However, the formation of graphite flakes directly influences the fraction of pearlite developed in gray iron, as both microstructural constituents compete for the available carbon. For graphite to precipitate, heterogeneous nuclei must first form, primarily consisting of MnS inclusions, which act as the main nucleation sites for graphite because of the low crystallographic mismatch between the two phases (33).

Figure 2 presents SEM micrographs of the GI1, GI2, and GI3 systems, in which MnS inclusions were identified. Quantitative analysis revealed a higher density of these nucleation sites in the GI3 system, with 226 ± 4.6 MnS/mm², compared with 101 ± 4.2 and 122 ± 2.7 MnS/mm² for GI1 and GI2, respectively. The increased MnS density is primarily associated with the concentrations of Mn, S, and microinclusions, which are commonly oxide-based.

The formation of complex MnS inclusions, which subsequently serve as nucleation sites for graphite, requires the prior presence of microinclusions typically composed of deoxidizing elements such as Si, Al, Ca, Ti, Zr, Ba, and Sr. These particles act as substrates for the nucleation and growth of MnS inclusions. Once MnS inclusions have formed, graphite preferentially nucleates and grows along crystallographic planes that minimize lattice distortion, leading to the development of eutectic cells (29).

For this reason, inoculation is a critical process in iron foundries, as inoculating agents are added to increase the number of graphite nucleation sites, reduce undercooling, and promote the formation of a favorable microstructure (29). In addition to inoculation, conditioning materials may also influence the microstructure through their impurity content and their contribution to the final chemical composition of the melt. Dwulat and Janerka (34). suggested that the

quality of conditioning materials, including their impurity content, may affect the formation of microinclusions that subsequently act as graphite nucleation sites.

Therefore, SEM characterization of the impurities (ash) in metallurgical graphite, electrode graphite and metallurgical coke was carried out in order to determine their main constituents. The results obtained are shown in Figures 3, 4 and 5.

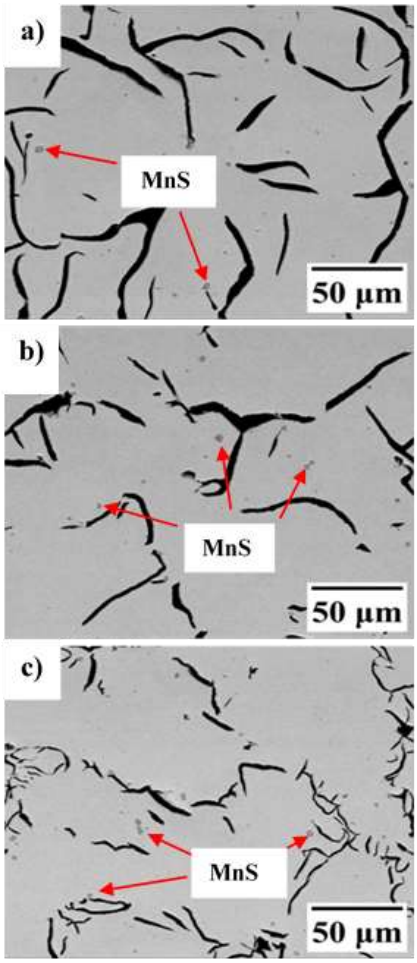

Figure 2. SEM images of the different irons: a) GI1, b) GI2, c) GI3.

The analysis revealed that the impurities were primarily composed of O, Si, Al, Ca, and Fe, elements commonly associated with heterogeneous nucleation phenomena in gray cast irons. These oxide-based particles can act as preferential substrates for MnS precipitation during solidification. Therefore, the higher MnS inclusion density observed in GI3 is likely associated with the combined influence of the higher impurity content and sulfur contribution of the metallurgical coke, together with the resulting lower Mn/S ratio. Under these conditions, a greater number of effective MnS nucleation sites could be generated, favoring graphite nucleation and contributing to the refinement of the pearlitic microstructure.

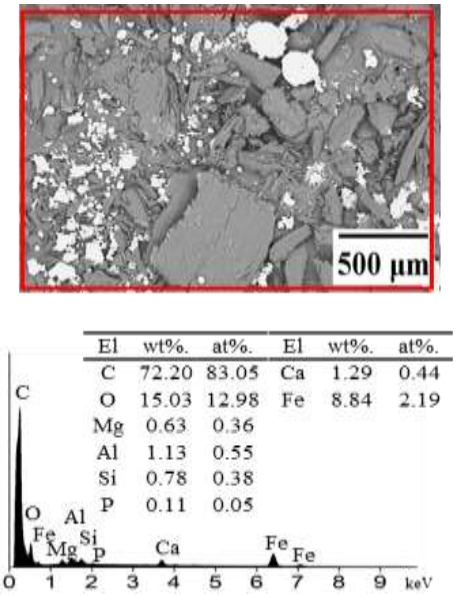

Figure 3. SEM and EDS images of metallurgical graphite ash.

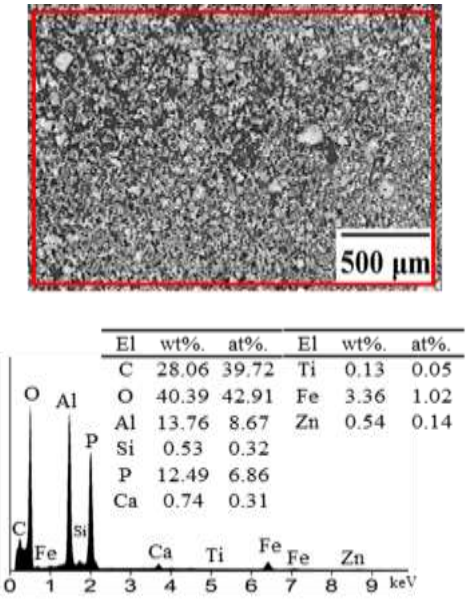

Figure 4. SEM and EDS images of graphite electrode ash.

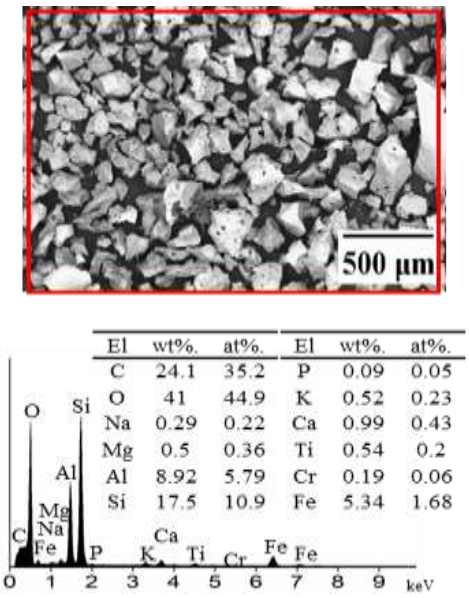

Figure 5. SEM and EDS images of metallurgical coke ash.

Smaller interlamellar spacing resulting from a finer pearlitic microstructure improves corrosion resistance by promoting a more uniform distribution of microgalvanic pairs (35).

Figure 6 shows images of fine pearlite in the different gray irons. The interlamellar spacing of fine pearlite ranged from 120 to 260 nm. The average interlamellar spacings were 173 ± 4.2 nm for GI1, 193 ± 3.8 nm for GI2, and 170 ± 3.5 nm for GI3, as summarized in Table 3. These values are comparable to those reported by Siswanto et al. (36), who observed a reduction in pearlite interlamellar spacing from 203 to 169 nm by increasing the Cu content from 0.3 to 0.4 wt.%, indicating that variations in alloy chemistry can significantly influence pearlite refinement. Likewise, in the present study, the smaller interlamellar spacing observed in GI3 is interpreted as the result of the combined influence of the selected preconditioning material and the associated differences in chemical composition. In particular, the higher sulfur content and the lower Mn/S ratio favored the formation of a greater density of MnS inclusions, which promoted graphite nucleation during solidification, while the slight variation in carbon equivalent may also have contributed to the eutectic solidification behavior and the subsequent pearlitic transformation. Therefore, the refined pearlitic microstructure observed in GI3 should be interpreted as the consequence of the combined metallurgical conditions generated by the selected preconditioning material rather than the effect of a single isolated variable.

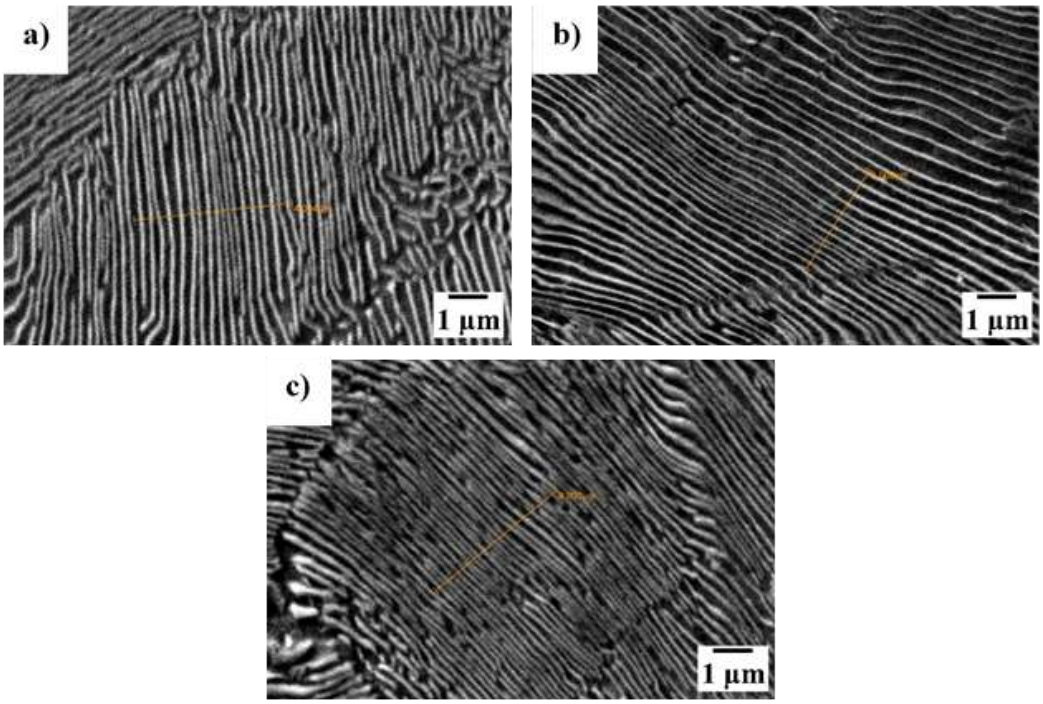

Figure 6. SEM images of fine pearlitic microstructure a) GI1, b) GI2 and c) GI3.

Table 3. Interlamellar spacing of fine pearlite in the different gray iron systems.

Gray iron	Average interlamellar spacing (nm)
GI1	173 ± 4.2
GI2	193 ± 3.8
GI3	170 ± 3.5

4.1.2 Corrosion resistance analysis

The polarization curves obtained from potentiodynamic tests conducted in a 3.5 wt.% NaCl solution are presented in Figure 7. The anodic and cathodic branches were analyzed using the Tafel extrapolation method to determine the corrosion potential (Ecorr) and corrosion current density (Icorr), the values of which are summarized in Table 4. The gray irons investigated exhibited Ecorr values ranging from −0.689 to −0.761 V, which are typical for ferrous materials of this type (17).

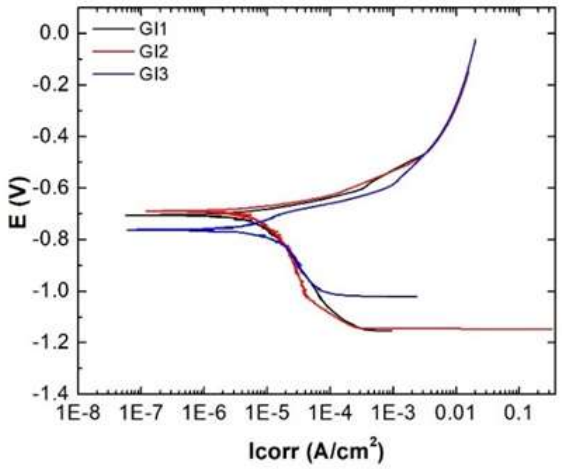

Figure 7. Polarization curves for GI1, GI2, and GI3.

Based on the Icorr values, the corrosion rate can be calculated and expressed in millimeters per year (mm/year) (37). Among the evaluated alloys, GI3 exhibited the lowest corrosion current density and, consequently, the lowest corrosion rate. The corrosion resistance followed the order GI3 > GI1 > GI2, corresponding to the inverse trend observed for corrosion rate (GI3 < GI1 < GI2), as illustrated in Figure 8.

The improved corrosion behavior observed for GI3 is consistent with the refined microstructure developed under the evaluated processing conditions, which was characterized by the highest density of MnS inclusions, the greatest fraction of fine pearlite, and the smallest average pearlite interlamellar spacing. These microstructural characteristics are expected to reduce local electrochemical heterogeneities and promote a more uniform corrosion process, thereby contributing to the lower corrosion rate observed for this alloy (17, 37). It should be noted, however, that this behavior cannot be attributed exclusively to the selected preconditioning material. As discussed in the previous sections, the different preconditioning materials also produced slight variations in sulfur content, Mn/S ratio, and carbon equivalent, which are expected to influence the solidification behavior and the resulting microstructure. Therefore, the superior electrochemical performance of GI3 is more appropriately interpreted as the combined effect of these metallurgical variables rather than the consequence of a single processing factor.

For comparison, A. H. Seikh et al. (18) reported an Icorr value of 70 μA/cm² for conventional gray cast iron, which decreased to approximately 7 μA/cm² after austempering heat treatment, demonstrating a significant improvement in corrosion resistance. Similarly, Bruna et al. (17) reported enhanced corrosion resistance through Cu and Ni alloying, obtaining the lowest corrosion rate of approximately 0.097 mm/year with 1 wt.% Cu. In the present study, GI3 exhibited a corrosion rate of 0.016 mm/year. Although direct comparison among different investigations should be made with caution because of differences in alloy composition, processing conditions, and electrochemical testing procedures, the corrosion rate obtained for GI3 is lower than those reported in the cited studies. These results suggest that the metallurgical conditions developed during processing were favorable for improving corrosion resistance without requiring additional alloying additions or post-solidification heat treatments.

Table 4. Quantification of potentiodynamic test results.

Gray iron	Ecorr (V)	Icorr (μA/cm²)	Corrosion rate (mm/year)
GI1	-0.704	5.130 ± 0.080	0.044 ± 0.004
GI2	-0.689	5.380± 0.080	0.046 ± 0.004
GI3	-0.761	1.820 ± 0.050	0.016 ± 0.002

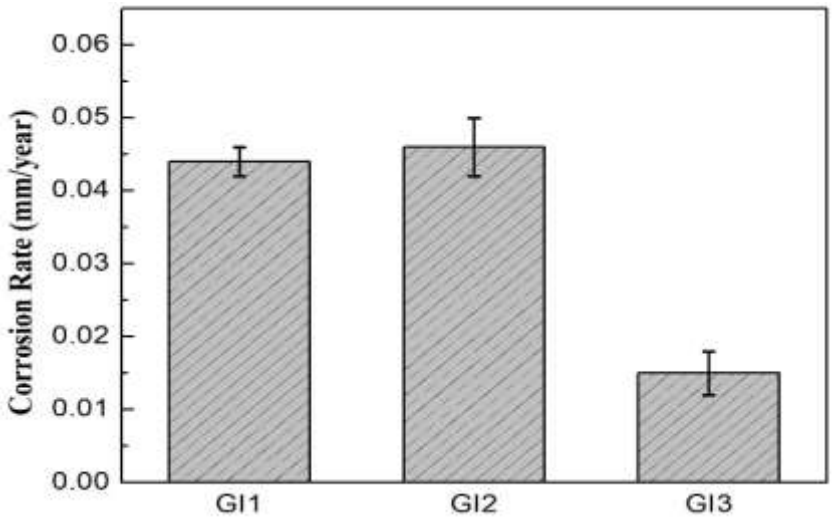

Figure 8. Corrosion rates for GI1, GI2, and GI3.

4.1.3 Microstructural analysis after corrosion

Figure 9 presents SEM images of the different gray irons after corrosion testing. GI1 exhibited the most severe surface corrosion, followed by GI2, whereas GI3 showed the least damage. These observations are consistent with the results obtained from the potentiodynamic polarization tests.

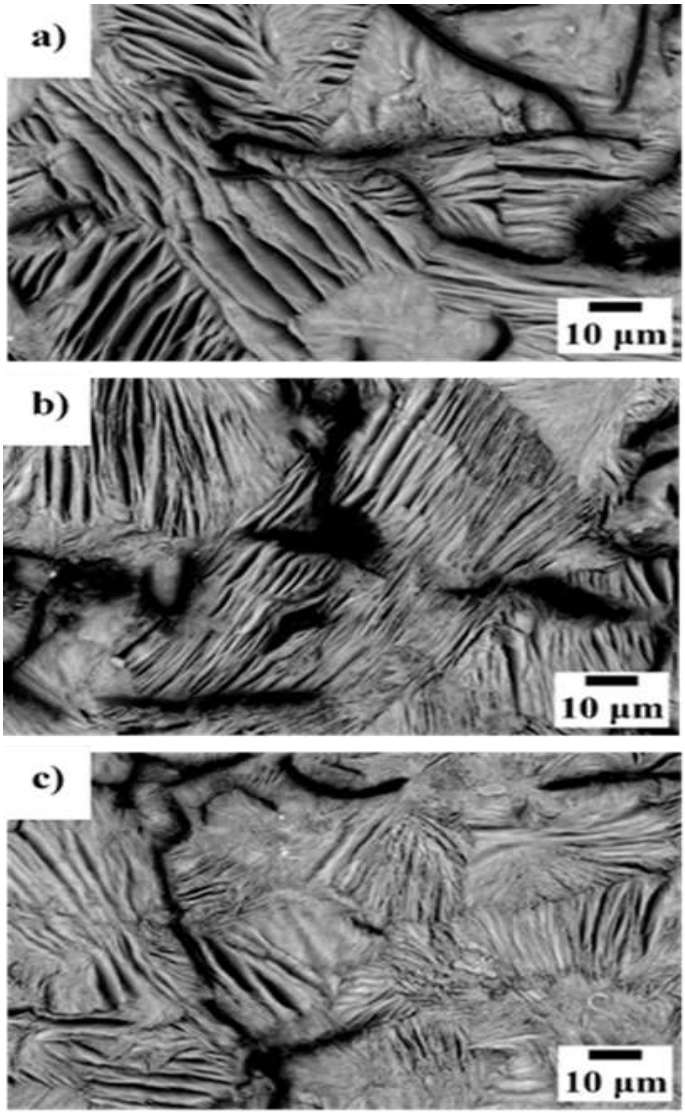

Figure 9. SEM images of the gray irons after corrosion: a) GI1, b) GI2, and c) GI3.

4.1.4 Statistical analysis of microstructural and corrosion results

The statistical analysis results are summarized in Table 5. ANOVA revealed statistically significant differences among the GI1, GI2, and GI3 systems for all evaluated microstructural and electrochemical parameters ($p < 0.05$). Among the variables analyzed, MnS inclusion density showed the greatest differences among the evaluated gray iron systems, followed by corrosion current density, indicating that the metallurgical conditions developed during processing significantly influenced both the microstructural evolution and the corrosion behavior.

Table 5. Statistical analysis of the microstructural and electrochemical parameters.

Parameter	Calculated F-value	p-value	Statistical significance
Fine pearlite (%)	57.69	6.99×10^{-7}	Yes ($p < 0.05$)
Inclusions (MnS/mm²)	1445.27	4.99×10^{-15}	Yes ($p < 0.05$)
Interlamellar spacing of fine pearlite (nm)	56.29	7.99×10^{-7}	Yes ($p < 0.05$)
Icorr (μA/cm²)	3961.91	1.20×10^{-17}	Yes ($p < 0.05$)
Corrosion rate (mm/year)	119.35	1.20×10^{-8}	Yes ($p < 0.05$)

As summarized in Table 6, the GI3 system exhibited the highest MnS inclusion density (226 ± 4.6 MnS/mm²), the largest fraction of fine pearlite (55.35 ± 0.84%), and the smallest interlamellar spacing of fine pearlite (170 ± 3.5 nm). These microstructural characteristics were associated with the lowest corrosion current density (1.82 ± 0.05 μA/cm²) and corrosion rate (0.016 ± 0.002 mm/year), demonstrating the influence of the metallurgical conditions developed during processing on the resulting microstructure and electrochemical behavior.

Compared with GI2, the GI3 system achieved an approximately 65% reduction in corrosion rate. This improvement is consistent with the higher density of MnS inclusions, which promoted graphite nucleation and pearlite refinement during solidification. Together with the slight differences in sulfur content, Mn/S ratio, and carbon equivalent discussed previously, these factors contributed to a more homogeneous microstructure, reducing local electrochemical heterogeneities and mitigating the formation of galvanic microcells.

Table 6. Microstructural and electrochemical parameters of the gray cast iron systems.

Gray iron	Fine Pearlite (%)	Inclusions (MnS/mm²)	Interlamellar spacing of fine pearlite (nm)	Icorr (μA/cm²)	Corrosion Rate (mm/year)
GI1	51.00 ± 0.87	101 ± 4.2	173 ± 4.2	5.13 ± 0.08	0.044 ± 0.004
GI2	49.18 ± 1.08	122 ± 2.7	194 ± 3.8	5.38 ± 0.08	0.046 ± 0.004
GI3	55.35 ± 0.84	226 ± 4.6	170 ± 3.5	1.82 ± 0.05	0.016 ± 0.002

The experimental comparison was based on the material used for preconditioning. All three heats followed the same melting procedure, while specimen preparation, metallographic examination, and electrochemical testing were performed in the same manner. The preconditioning materials did not have identical compositions or purity levels. Consequently, their addition introduced small differences in the final alloy chemistry. These differences formed part of the overall effect associated with each material, even though the remaining processing and testing conditions were kept constant.

One heat was produced for each preconditioning condition. Three specimens were prepared from every heat and used for the microstructural and electrochemical

evaluations. The quantitative microstructural data were obtained from ten measurements distributed among the three specimens. The electrochemical values represent the mean of five potentiodynamic polarization tests for each condition. Since no additional heats were produced, the measurements describe variation within each heat but do not account for possible differences between separate heats prepared with the same material. The ANOVA results in Table 5 identified significant differences among the three conditions and support the trends observed in this experiment. They do not, however, establish whether the same magnitude of difference would be reproduced in other heats. Future work should include replicate heats for every preconditioning material to assess this source of variation.

5. Conclusions

The three preconditioning materials did not produce exactly the same alloy chemistry. Small differences were measured in sulfur content, carbon equivalent, and the balance between manganese and sulfur. Since each of these variables can affect solidification, they were taken into account when comparing the microstructures.

The most refined microstructure was observed in the gray iron prepared with metallurgical coke. Its MnS inclusion density reached 226 ± 4.6 MnS/mm², which was the highest value among the three conditions. Fine pearlite accounted for 55.35 ± 0.84% of the evaluated microstructure, while the measured interlamellar spacing was 170 ± 3.5 nm. No other condition showed a larger fraction of fine pearlite or a smaller spacing between pearlite lamellae. These measurements show that the microstructure obtained with metallurgical coke was finer than those produced with metallurgical graphite and electrode graphite.

The electrochemical results followed a similar trend. The alloy produced with metallurgical coke had the lowest corrosion current density and a corrosion rate of 0.016 ± 0.002 mm/year. This rate was approximately 65% lower than that measured for the alloy produced with electrode graphite. The ANOVA results showed statistically significant differences among the evaluated conditions ($p < 0.05$).

The improvement observed in the alloy produced with metallurgical coke cannot be attributed to a single factor. Its corrosion response was accompanied by differences in sulfur content, Mn/S ratio, carbon equivalent, MnS inclusion density, and pearlite refinement. Since the contribution of each variable was not evaluated independently, the effect of any one of them could not be quantified. Nevertheless, their combined variation was associated with the microstructural and electrochemical differences measured among the three gray irons.

In this experiment, preconditioning affected more than the adjustment of carbon content. The selected material was also related to changes in solidification, microstructure, and corrosion behavior. The results suggest that an appropriate choice of preconditioning material may help improve the corrosion resistance of gray cast iron without additional alloying elements or heat treatments after solidification.

6. Acknowledgements

The authors would like to thank the Tecnológico Nacional de México (TecNM) / Instituto Tecnológico de Saltillo and the Secretaría de Ciencia, Humanidades, Tecnología e Innovación (SECIHTI) for their financial support in the form of a doctoral scholarship (CVU 998922), and the Sistema Nacional de Investigadoras e Investigadores

(SNII) for its support in the development of this project.

7. References

1. ACEA (2025) Economic and Market Report Global and EU auto industry: Full year 2024. *Acea*.

2. de Souza, A., de Oliveira-Júnior, J.F., Cardoso, K.R.A. and Gautam, S. (2025) Impact of vehicular emissions on ozone levels: A comprehensive study of nitric oxide and ozone interactions in urban areas. *Geosystems and Geoenvironment*, **4**, 100348. https://doi.org/10.1016/j.geogeo.2024.100348

3. Al-Sabbagh, T.A. and Shreaz, S. (2025) Impact of Lead Pollution from Vehicular Traffic on Highway-Side Grazing Areas: Challenges and Mitigation Policies. *Int. J. Environ. Res. Public Health*, **22**, 1–30. https://doi.org/10.3390/ijerph22020311 http://www.ncbi.nlm.nih.gov/pubmed/40003536

4. Selvi, M.S. and Önem, Ş. (2025) Impact of Variables in the UTAUT 2 Model on the Intention to Use a Fully Electric Car. *Sustainability (Switzerland)*, **17**, 1–24. https://doi.org/10.3390/su17073214

5. Alvarez-Diazcomas, A., Estévez-Bén, A.A., Rodríguez-Reséndiz,J., Carrillo-Serrano,R. V. and Álvarez-Alvarado,J.M. (2023) A High-Efficiency Capacitor-Based Battery Equalizer for Electric Vehicles. *Sensors*, **23**, 1–16. https://doi.org/10.3390/s23115009 http://www.ncbi.nlm.nih.gov/pubmed/37299739

6. Szumska, E.M. (2025) Regenerative Braking Systems in Electric Vehicles: A Comprehensive Review of Design, Control Strategies, and Efficiency Challenges. *Energies (Basel).*, **18**. https://doi.org/10.3390/en18102422

7. Jamadar, N.M. and Jadhav, H.T. (2021) Rule-based assistive hybrid electric brake system with energy generation for electric vehicle. *Energy Sources, Part A: Recovery, Utilization and Environmental Effects*, **43**, 1–19. https://doi.org/10.1080/15567036.2021.2015485

8. Gweon, J., Shin, S., Jang, H., Lee, W., Kim, D. and Lee, K. (2018) The Factors Governing Corrosion Stiction of Brake Friction Materials to a Gray Cast Iron Disc. *SAE Technical Papers*, **2018-Octob**, 5–12. https://doi.org/10.4271/2018-01-1899

9. Gweon, J., Park, J., Kyu, W., Yeon, D. and Jang, H. (2021) Root cause study of corrosion stiction by brake pads on the grey iron disc. *Eng. Fail. Anal.*, **128**, 1–13. https://doi.org/10.1016/j.engfailanal.2021.105583

10. Motta, M., Fedrizzi, L. and Andreatta, F. (2023) Corrosion Stiction in Automotive Braking Systems. *Materials*, **16**. https://doi.org/10.3390/ma16103710

11. Mao, F., He, Y., Guo, A., Wang, X., Zhong, Y., Huang, Z., Chen, C. and Wei, S. (2025) Effect of vanadium and temperature on the tribological properties of gray cast iron. *Journal of Materials Research and Technology*, **38**, 3578–3590. https://doi.org/10.1016/j.jmrt.2025.08.211

12. Kumar, A., Pandey, R., Kumar, R., Kumar, N. and Kiran, T.R. (2021) Materials Today: Proceedings Thermal analysis on car brake rotor using cast iron material with different geometries. *Mater. Today Proc.*, 10.1016/j.matpr.2021.05.299. https://doi.org/10.1016/j.matpr.2021.05.299

13. Liu, Y., Lee, H., Hess, D. and Coryell, J. (2025) Thermomechanical Fatigue Behavior of Gray Cast Iron in Brake Rotors. In *SAE Technical Papers*. https://doi.org/10.4271/2025-01-8319

14. Wang, Y., Shuai, S. and Ge, Y. (2025) Controlling brake particle emissions: New brake disc needs more attention. *Results in Engineering*, **27**, 107120. https://doi.org/10.1016/j.rineng.2025.107120

15. Catapano, F., Iorio, S. Di, Magno, A., Sequino, L. and Vaglieco, B.M. (2025) Brake particle emissions: Effect of temperature and modeling of temperature behavior. *Results in Engineering*, **26**, 104872. https://doi.org/10.1016/j.rineng.2025.104872

16. Gonet, T. and Maher, B.A. (2019) Airborne, Vehicle-Derived Fe-Bearing Nanoparticles in the Urban Environment: A Review. *Environ. Sci. Technol.*, **53**, 9970–9991. https://doi.org/10.1021/acs.est.9b01505 http://www.ncbi.nlm.nih.gov/pubmed/31381310

17. Bruna, H., Allende-Seco, R., Artigas, A., Monsalve, A. and Sánchez, C. (2024) Effect of Copper and Nickel Content on the Corrosion Mechanisms in Ferritic Matrix Gray Cast Irons under Simulated Marine Environments. *Metals (Basel).*, **14**. https://doi.org/10.3390/met14060696

18. Seikh, A.H., Sarkar, A., Singh, J.K., Mohammed, S.M.A.K., Alharthi, N. and Ghosh, M. (2019) Corrosion characteristics of copper-added austempered gray cast iron (AGCI). *Materials*, **12**, 1–17. https://doi.org/10.3390/ma12030503

19. Godwin, I., Sunday, O., Fayomi, I. and Nwankwo, P. (2023) Investigation of the microstructure, corrosion resistance and hardness of bone particle reinforced cast iron for engine blocks application in automotive and marine industries. **2**.

20. Dwulat, R., Janerka, K., Grzesiak, K. and Gałuszka, M. (2023) Influence of Charge Materials on the Metallurgical Quality of Gray Cast Iron. *Archives of Foundry Engineering*, **23**, 66–71. https://doi.org/10.24425/afe.2023.144297

21. Futas, P., Pribulova, A., Petrik, J., Blasko, P., Junakova, A. and Sabik, V. (2023) Metallurgical Quality of Cast Iron Made from Steel Scrap and Possibilities of Its Improvement. *Metals (Basel).*, **13**, 1–10. https://doi.org/10.3390/met13010027

22. Scherbring, S., Adams, B. and Mola, J. (2024) Impact of interlamellar spacing and non-pearlitic features on mechanical properties and cyclic damage initiation in near-eutectoid pearlitic steels. *Materials Science and Engineering: A*, **889**. https://doi.org/10.1016/j.msea.2023.145846

23. Genculu, S. (2024) Cast Irons -Properties and Applications. *CAB worldwide*.

24. Srivastava, R., Singh, B. and Saxena, K.K. (2019) Influence of S and Mn on mechanical properties and microstructure of grey cast iron: An overview. *Mater. Today Proc.*, **26**, 2770–2775. https://doi.org/10.1016/j.matpr.2020.02.577

25. De Santiago-Méndez, L.F., Castro-Román, M. de J., Herrera-Trejo, M., Mancha-Molinar, H. and Bravo, B. (2025) Influence of S and Mn Initial Concentrations on the Graphite Branching in Gray Cast Iron as Quantified by 2D Image Analysis. *Materials*, **18**. https://doi.org/10.3390/ma18214837

26. Stefan, E., Chisamera, M., Riposan, I. and Stan, S. (2021) Graphite nucleation sites in commercial gray cast irons. *Materials Today: Proceedings*, **45**, 4091-4095. https://doi.org/10.1016/j.matpr.2020.11.009

27. Lima, M.L., Albertin, E., Correa, E.R., Rabello, R.B. and Uehara, S. (2020) Pearlite Refining Strategies for Hypoeutectic Gray Cast Iron. *International Journal of Metalcasting*, **14**, 766–773. https://doi.org/10.1007/s40962-020-00413-6

28. Roučka, J., Prochazka, J., Kana, V., Krutis, V. and Nedelova, K. (2019) The influence of lamellar graphite cast iron annealing on hardness and structure. *Archives of Foundry Engineering*, **19**, 105–112. https://doi.org/10.24425/afe.2019.129639

29. Stefanescu, D.M., Alonso, G., Larrañaga, P. and Suarez, R. (2016) On the stable eutectic solidification of iron-carbon-silicon alloys. *Acta Mater.*, **103**, 103–114. https://doi.org/10.1016/j.actamat.2015.09.043

30. Alloys, I. (2020) Recent Developments in Understanding Nucleation and Crystallization of Spheroidal Graphite in.

31. Eiken, J. (2020) Calphad-based phase-field study of the interplay between spheroidal graphite growth and chemical segregation in ductile cast iron Calphad-based phase-field study of the interplay between spheroidal graphite growth and chemical segregation in ductile cast. *Materials Science and Engineering*, **861**, 1–8. https://doi.org/10.1088/1757-899X/861/1/012055

32. Yin, R. yu (2021) Review on the study of metallurgical process engineering. *International Journal of Minerals, Metallurgy and Materials*, **28**. https://doi.org/10.1007/s12613-020-2220-z

33. Ştefănescu, D.M., Alonso, G., Larrañaga, P., De La Fuente, E. and Suarez, R. (2018) Reassessment of crystal growth theory of graphite in cast iron. *Materials Science Forum*, **925 MSF**, 36–44. https://doi.org/10.4028/www.scientific.net/MSF.925.36

34. Dwulat, R. and Janerka, K. (2023) Evaluation of the Metallurgical Quality of Nodular Cast Iron in the Production Conditions of a Foundry. *Journal of Manufacturing and Materials Processing*, **7**. https://doi.org/10.3390/jmmp7010018

35. Wang, Z., Zhang, X., Yu, H., Liu, J., Cheng, L., Hu, S.E. and Wu, K. (2022) Effects of pearlite on corrosion initiation and propagation in weathering steels in marine environments. *J. Mater. Sci.*, **57**, 6039–6055. https://doi.org/10.1007/s10853-022-07001-5

36. Siswanto, A., Widodo, R. and Ardiansyah, E. (2020) Effect of interlamellar spacing on tensile strength gray cast iron with copper variations. *J. Phys. Conf. Ser.*, **1450**. https://doi.org/10.1088/1742-6596/1450/1/012127

37. Zhang, Y., Feng, X., Huang, Q., Li, Y., Hao, X. and Wang, C. (2023) The corrosion characteristics and mechanism of directionally solidified Mg-3Zn-xCa alloys. *Journal of Magnesium and Alloys*, **11**, 3673–3687. https://doi.org/10.1016/j.jma.2022.02.010